

# Fractal Superconducting Nanowires Detect Infrared Single Photons with 84% System Detection Efficiency, 1.02 Polarization Sensitivity, and 20.8 ps Timing Resolution

Yun Meng, Kai Zou, Nan Hu, Liang Xu, Xiaojian Lan, Stephan Steinhauer, Samuel Gyger, Val Zwiller, and Xiaolong Hu\*



Cite This: *ACS Photonics* 2022, 9, 1547–1553



Read Online

ACCESS |



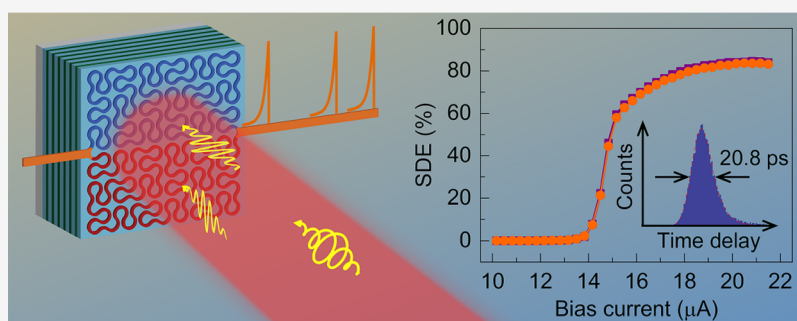
Metrics & More



Article Recommendations



Supporting Information



**ABSTRACT:** The near-unity system detection efficiency (SDE) and excellent timing resolution of superconducting nanowire single-photon detectors (SNSPDs), combined with their other merits, have enabled many classical and quantum photonic applications. However, the prevalent design based on meandering nanowires makes SDE dependent on the polarization states of the incident photons; for unpolarized light, the major merit of high SDE would get compromised, which could be detrimental to photon-starved applications. Here, we create SNSPDs with an arced fractal geometry that almost completely eliminates this polarization dependence of the SDE, and we experimentally demonstrate  $84 \pm 3\%$  SDE,  $1.02^{+0.06}_{-0.02}$  polarization sensitivity at the wavelength of 1575 nm, and 20.8 ps timing jitter in a 0.1 W closed-cycle Gifford–McMahon cryocooler, at the base temperature of 2.0 K. This demonstration provides a novel, practical device structure of SNSPDs, allowing for operation in the visible, near-infrared, and mid-infrared spectral ranges, and paves the way for polarization-insensitive single-photon detection with high SDE and high timing resolution.

**KEYWORDS:** superconducting nanowire single-photon detectors, fractal, timing jitter, current crowding, photon counters, quantum optics

## INTRODUCTION

Because of their near-unity system detection efficiency (SDE),<sup>1–7</sup> low dark-count rate (DCR),<sup>8</sup> high count rate,<sup>9–12</sup> excellent timing resolution,<sup>13,14</sup> and broad working spectral range,<sup>15–18</sup> superconducting nanowire single-photon detectors (SNSPDs)<sup>19</sup> have been widely used in classical and quantum photonic applications,<sup>20</sup> ranging from LiDAR,<sup>21</sup> detection of luminescence from singlet oxygen,<sup>22</sup> and quantum key distribution (QKD)<sup>23</sup> to quantum computing.<sup>24,25</sup> Indeed, these detectors have become indispensable tools and enabling components in the systems requiring faint-light detection. However, the prevalent design based on meandering nanowires yields polarization-dependent SDE, which could be problematic if information is encoded in polarization states. In particular, when the polarization states of the photons are unknown, time-varying, or random, it may not be possible to rotate the polarization states to maximize the SDE of SNSPDs. Therefore, the major merit of these detectors would get

severely compromised, and this compromise could be detrimental to many photon-starved applications that stringently require high SDE. For photon-number-resolving detection or coincidence photon counting, the fidelity to resolve  $n$  photons or the  $n$ -fold coincidence count rate scales with  $\text{SDE}^n$ ,<sup>26,27</sup> which quickly drops if the SDE decreases. In a QKD system using SNSPDs, the polarization-dependent mismatch of SDE makes the system vulnerable to quantum hacking.<sup>28</sup> Furthermore, the subtle trade-offs between the SDE and timing resolution<sup>29</sup> make their simultaneous optimization challenging. Recently, 85% SDE at the wavelength of 915 nm

Received: May 17, 2021

Published: April 13, 2022



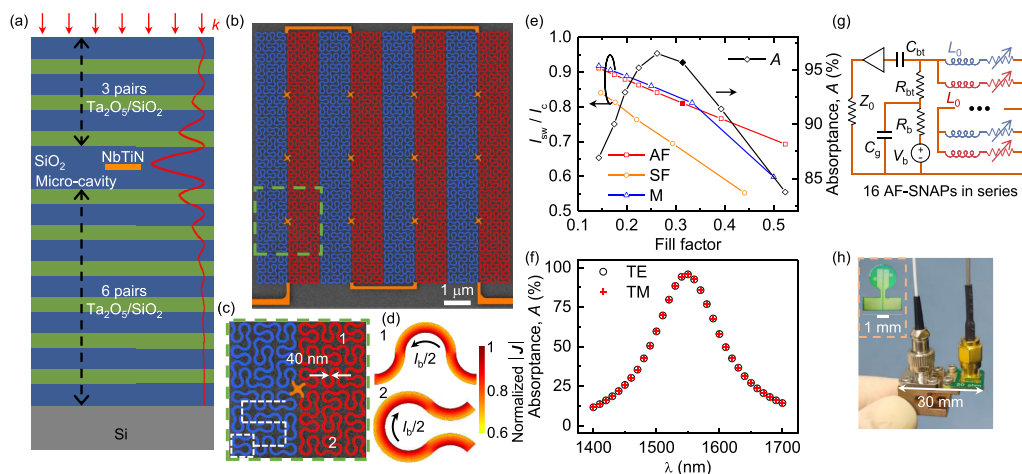


**Figure 1.** Design, fabrication, and packaging of arced fractal SNAPs (AF-SNAPs). (a) Schematic of the optical structure of an AF-SNAP. The nanowire is sandwiched in an optical microcavity supported by distributed Bragg structures, which are composed of dielectric alternating layers of silicon dioxide ( $\text{SiO}_2$ ) and tantalum pentoxide ( $\text{Ta}_2\text{O}_5$ ). The detector is illuminated from top, and the red line presents the simulated distribution of the light intensity, assuming the absence of the nanowire. The nanowire is positioned in the microcavity, where the light intensity is the strongest. (b) False-colored scanning-electron micrograph of an AF-SNAP, in which the photosensitive nanowires are colored in red and blue, and the auxiliary structures are colored in orange. (c) Zoom-in micrograph of the region enclosed in the green-dashed box in (b). The width of the nanowire was measured to be 40 nm. (d) Simulated and normalized distribution of supercurrent density,  $|J|$ , at the proximity of an L-turn and a U-turn, denoted in (c) as 1 and 2, respectively. (e) Simulated normalized switching currents,  $I_{\text{sw}}/I_c$ , of the arced fractal (red), standard fractal (orange), and meandering (blue) nanowires, as functions of the fill factor. The simulated optical absorbance (black) of the arced fractal nanowire is also presented as a function of the fill factor. The fill factor used in this work is 0.31. (f) Simulated optical absorbance of the AF-SNAP for two orthogonal linear polarization states, transverse-electric (TE) and transverse-magnetic (TM) states, as functions of the wavelength,  $\lambda$ . (g) Equivalent circuitry of the AF-SNAP, which is composed of 16 cascaded 2-SNAPs. (h) Photograph of the chip package. Inset: a photograph of the keyhole-shaped chip.

with 7.7 ps device timing jitter<sup>14</sup> and 98% SDE at the wavelength of 1425 nm with 26 ps system timing jitter<sup>6</sup> were demonstrated on meandering SNSPDs, but the SDEs were still polarization-dependent.

To address the issue of polarization dependence of the SDE, several approaches have been proposed and demonstrated, including spiral SNSPDs,<sup>30,31</sup> two orthogonal side-by-side meanders,<sup>30</sup> double-layer orthogonal meanders,<sup>32</sup> SNSPDs involving compensating high-index materials,<sup>33,34</sup> specially designed SNSPDs with a low polarization dependence at a certain wavelength,<sup>4,35</sup> and fractal SNSPDs.<sup>29,36,37</sup> These demonstrations all have successfully reduced the polarization sensitivity (PS, the ratio of the polarization-maximum SDE,  $\text{SDE}_{\text{max}}$  and over the polarization-minimum SDE,  $\text{SDE}_{\text{min}}$ ) of SNSPDs; however, none of them could simultaneously preserve other major merits, in particular, high SDE and excellent timing resolution. Among these demonstrations, amorphous SNSPDs, made of WSi or MoSi, have exhibited over 80%<sup>32,35</sup> and even over 90% SDE;<sup>4</sup> however, their timing jitter ranges from 76 to 465 ps; on the other hand, polycrystalline SNSPDs, made of NbN or NbTiN, have shown a better timing resolution; however, so far, the highest SDE demonstrated on polycrystalline SNSPDs with low-PS designs is 60%,<sup>29</sup> still significantly lower than the state-of-the-art  $\text{SDE}_{\text{max}}$  of meandering SNSPDs, which is over 90% demonstrated by several research groups.<sup>1–7</sup> Therefore, it remains an outstanding challenge how to boost the SDE of SNSPDs with a low PS to the level comparable to the  $\text{SDE}_{\text{max}}$  of their meandering counterparts while simultaneously optimizing the timing resolution.

Although the geometry of the fractal SNSPDs<sup>29,37</sup> eliminated the global orientation of the nanowire and therefore significantly reduced the PS, it was also this geometry that

brought the major obstacle for further enhancing the SDE and timing resolution. The fractal design contains a plethora of U-turns and L-turns that may limit the switching current,  $I_{\text{sw}}$ , due to the current-crowding effect,<sup>39</sup> which may further affect the SDE and timing resolution. In the past, we demonstrated fractal superconducting nanowire avalanche photodetectors (SNAPs)<sup>29</sup> with 60% SDE, 1.05 PS, and 45 ps timing jitter. However, it is still elusive whether this route, using fractal geometry, is a practical one to combine high SDE, low PS, and low timing jitter.

In this paper, we report on our design and demonstration of a fiber-coupled fractal SNAP, fully packaged in a 0.1 W closed-cycle Gifford–McMahon (GM) cryocooler with a base temperature of 2.0 K, achieving  $84 \pm 3\%$  SDE,  $1.02^{+0.06}_{-0.02}$  PS at a wavelength of 1575 nm, and 20.8 ps timing jitter. An enabling innovation is that we used an arced fractal geometry<sup>40</sup> for the nanowire to successfully reduce the current-crowding effect and, therefore, increased  $I_{\text{sw}}$  to a level comparable to that in the meandering structure with the same nanowire width, thickness, and fill factor, achieving saturated, near-unity internal quantum efficiency,  $P_r$ . We integrated the arced fractal nanowire with an optical microcavity, supported by dielectric distributed Bragg structures, for enhancing the optical absorbance,  $A$ , of the nanowire.<sup>3,5,7,41</sup>

## RESULTS AND DISCUSSION

Figure 1a presents a schematic of the optical structure of an arced fractal SNAP (AF-SNAP). Six pairs of alternating silicon dioxide ( $\text{SiO}_2$ ) and tantalum pentoxide ( $\text{Ta}_2\text{O}_5$ ) layers were deposited on a silicon substrate, functioning as the bottom Bragg reflector; three pairs formed the top reflector; in between a  $\text{SiO}_2$  defect layer was sandwiched. The thicknesses of a  $\text{SiO}_2$  layer and a  $\text{Ta}_2\text{O}_5$  layer in the Bragg reflectors are

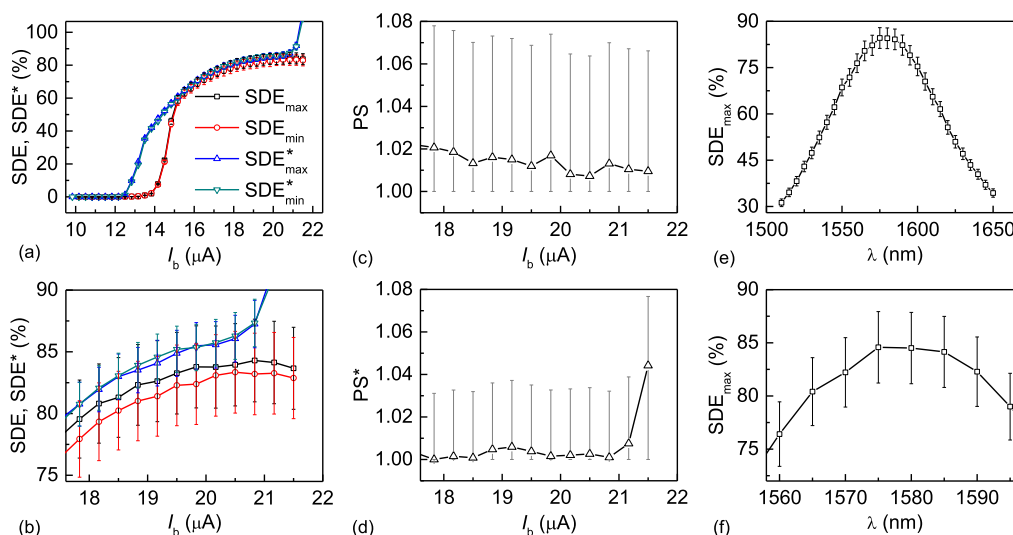


**Figure 2.** Measured SDE and polarization dependence of an arced fractal SNAP (AF-SNAP). (a) Measured SDE<sub>max</sub>, SDE<sub>min</sub>, SDE\*<sub>max</sub>, and SDE\*<sub>min</sub> as functions of the bias current,  $I_b$ . (b) Zoom-in view of (a) at the high-bias regime with  $I_b$  exceeding 17.5  $\mu\text{A}$ . (c) Polarization sensitivity, PS, calculated from the measured SDE<sub>max</sub> and SDE<sub>min</sub>. (d) Polarization sensitivity, PS\*, calculated from the measured SDE\*<sub>max</sub> and SDE\*<sub>min</sub>. (e) Measured spectrum of SDE<sub>max</sub> at a bias current of 21.17  $\mu\text{A}$ . (f) Zoom-in view of the SDE<sub>max</sub> spectrum near a central wavelength of 1575 nm.

264 and 180 nm, respectively; and the thickness of the SiO<sub>2</sub> defect layer is 529 nm, targeting for a wavelength of 1550 nm with optimal optical absorptance. The red line in Figure 1a shows the simulated distribution of the light intensity in the dielectric stacks (without the nanowires) at a wavelength of 1550 nm for top illumination; and the NbTiN nanowires were designed to locate in the middle of the defect layer of the optical microcavity, where the light intensity is the strongest. The thickness of the NbTiN film used in this work was 9 nm. Figure 1b presents a false-colored scanning-electron micrograph of a fabricated AF-SNAP, before the top Bragg layers were integrated. The photosensitive region of the detector was 10.2  $\mu\text{m}$  by 10.2  $\mu\text{m}$ , and the width of the nanowire was measured to be 40 nm [Figure 1c]. The photosensitive region of the detector is composed of 64 second-order arced fractal Peano curves<sup>40</sup> that are electrically connected according to the circuitry in Figure 1g. In comparison to the standard Peano fractal curve,<sup>29,37</sup> the arced Peano fractal curve<sup>40</sup> reduced the current-crowding effect at the turns. We simulated the normalized distribution of the supercurrent density,  $|J|$ , at the proximity of an L-turn and a U-turn [Section S1 of Supporting Information], which are presented in Figure 1d. Figure 1e further presents the simulated  $I_{sw}$ , normalized to the critical current of a straight nanowire with the same width and thickness,  $I_c$ , of the meandering, standard fractal, arced fractal nanowires as functions of the fill factor. We used a commercial software COMSOL Multiphysics based on the finite-element method for these simulations. At a fill factor of 0.31 used in this work, the simulated optical absorptance for the plane wave at a wavelength of 1550 nm is 96%, and the normalized switching current of the arced fractal nanowire is 0.81. As a comparison, with the same fill factor, 0.31, the normalized switching currents of the meandering nanowire and the standard fractal nanowire are 0.82 and 0.67, respectively, further evidencing that the current-crowding effect in the arced fractal nanowire is significantly reduced, compared with that in the standard fractal one. A detailed comparison of the distribution of the supercurrent density of these three types

of geometry is presented in Section S1 of Supporting Information. Figure 1f presents the simulated optical absorptance,  $A$ , of the AF-SNAP for the plane wave as functions of the wavelength for two orthogonal linear polarization states, denoted as transverse-electric (TE) and transverse-magnetic (TM) states.  $A$  peaks at 1550 nm and remains above 50% in the wavelength range from 1490 to 1610 nm. The simulation shows that  $A$  is completely polarization-independent. To investigate the coupling efficiency,  $\eta_c$ , we simulated the optical modes of the optical microcavity without the nanowires. The simulated mode-field diameter (MFD) at the plane of nanowires coupled with a Corning high-index optical fiber (HIF, HI 1060 FLEX) used in this paper was 6.8  $\mu\text{m}$ , which ensured a  $\eta_c$  of 99%, assuming perfect alignment. In comparison, the MFD at the plane of nanowires coupled with a Corning SMF-28e+ optical fiber (SMF) was 10.7  $\mu\text{m}$  and the corresponding coupling efficiency is 89%. The detector coupled with HIF is more tolerable to the spatial misalignment than the detector coupled with SMF. A detailed simulation regarding optical modes of the cavity is presented in Section S2 of Supporting Information. Electrically, the detector was composed of 16 cascaded 2-SNAPs, as we used previously,<sup>29</sup> and Figure 1g presents the equivalent circuit diagram. The chips were etched into the keyhole shape by the Bosch process for self-aligned packaging.<sup>42</sup> A detailed fabrication process is presented in Section S3 of the Supporting Information. Figure 1h shows a photograph of the resulting chip package and the inset presents a photograph of a keyhole-shaped chip. In this package, the detector was self-aligned and directly coupled with a HIF, with a MFD of  $6.3 \pm 0.3 \mu\text{m}$ , which was connected to the SMF, with a MFD of  $10.4 \pm 0.5 \mu\text{m}$ , through an in-line mode-field adapter (Section S4 of Supporting Information).

We used the experimental setup, schematically presented in Section S4 of Supporting Information, to measure SDE and the polarization dependence. The base temperature for these measurements was 2.0 K. At this temperature,  $I_{sw} = 21.67 \mu\text{A}$ . A cryogenic, low-noise microwave amplifier was mounted on the 40 K stage and used to amplify the output pulses. We first measured the DCR as a function of the bias current (Section

SS of Supporting Information). Then, we biased the detector at 21.17  $\mu\text{A}$ , tuned the laser wavelength, and found that the SDE peaked at 1575 nm for this particular detector. The wavelength deviation from the designed wavelength with the maximum optical absorptance is presumably due to deviations of the thicknesses of the deposited dielectric layers and the refractive indices. We then fixed the wavelength at 1575 nm and scanned the polarization states of the input light over the Poincaré sphere and found the polarization states corresponding to  $\text{SDE}_{\text{max}}^*$  and  $\text{SDE}_{\text{min}}^*$ ; at these two polarization states, we measured  $\text{SDE}_{\text{max}}^*$  and  $\text{SDE}_{\text{min}}^*$  as the functions of the bias current [Figure 2a]. To accurately measure the SDE\*, we calibrated each optical attenuator at each polarization state and each wavelength for these measurements (Section S6 of Supporting Information). In the high-bias regime ( $I_b > 20.17 \mu\text{A}$ ), as shown in Figure 2a,b, the  $\text{SDE}^* - I_b$  curves go upward, showing additional false counts other than the dark counts and showing an unrealistic SDE\*. Similar observations have previously been reported on meandering SNAPs<sup>43</sup> and also SNSPDs.<sup>44</sup> We re-measured the  $\text{SDE}_{\text{max}}$  and  $\text{SDE}_{\text{min}}$  using the method based on time-correlated photon counting<sup>44</sup> to exclude the false counts. Note that we use  $\text{SDE}^*$  to refer to the SDE directly measured with the CW laser [Figure S5a for the experimental setup], excluding the dark counts; and we use SDE to refer to the SDE measured by time-correlated photon counting, excluding all false counts [Figure S5b for the experimental setup]. The values of the SDE and  $\text{SDE}^*$  in Figure 2a,b,e,f take into account the fiber end-facet reflection that occurred when we used an optical power meter to measure the optical power coming out from the fiber to avoid under-calculating the optical power delivered to the cryogenic AF-SNAP system and, therefore, to avoid over-calculating SDE and  $\text{SDE}^*$  (Section S7 of Supporting Information). In Figure 2, the associated error bars present the uncertainties with 68% confidence ( $k = 1$ )<sup>45</sup> of the measurements (Section S8 in the Supporting Information). At a bias current of 19.83  $\mu\text{A}$ ,  $\text{SDE}_{\text{max}}$  was measured to be  $84 \pm 3\%$ ,  $\text{SDE}_{\text{min}}$  was measured to be  $82 \pm 3\%$ , and the resulting PS ( $\text{SDE}_{\text{max}}/\text{SDE}_{\text{min}}$ ) was  $1.02_{-0.02}^{+0.06}$ .  $\text{SDE}_{\text{max}}^*$  and  $\text{SDE}_{\text{min}}^*$  were measured to be both  $85 \pm 2\%$ , and the resulting  $\text{PS}^*$  was  $1.00_{-0}^{+0.03}$ . At this bias current, DCR and false-count rate (FCR) were measured to be  $2.1 \times 10^3$  and  $2.2 \times 10^3$  cps, respectively (Section S5 of Supporting Information). At a bias current of 17.83  $\mu\text{A}$ ,  $\text{SDE}_{\text{max}}$  and  $\text{SDE}_{\text{min}}$  decreased to  $80 \pm 3$  and  $78 \pm 3\%$ , respectively;  $\text{SDE}_{\text{max}}^*$  and  $\text{SDE}_{\text{min}}^*$  decreased to both  $81 \pm 2\%$  [Figure 2b]; and the measured FCR and DCR at this bias current were  $3.7 \times 10^2$  and  $3.0 \times 10^2$  cps, respectively. In the low-bias regime,  $I_b < 15.83 \mu\text{A}$ , the detector was unstable,<sup>46</sup> generating multiple false pulses with low amplitudes after detecting one photon [Section S9 of Supporting Information], and resulting in the pronounced deviation of  $\text{SDE}^*$  from the SDE. PS and  $\text{PS}^*$ , as functions of the bias current, were calculated and presented in Figure 2c,d. Figure 2e presents  $\text{SDE}_{\text{max}}$  as a function of the wavelength,  $\lambda$ , at a bias current of 21.17  $\mu\text{A}$ . The full width at half maxima (fwhm) of the spectrum of  $\text{SDE}_{\text{max}}$  is 110 nm, which is slightly smaller than the fwhm, 120 nm, of the designed spectrum of the optical absorptance [Figure 1f]. Figure 2f presents a zoom-in view of the  $\text{SDE}_{\text{max}}$  for the wavelengths ranging from 1560 to 1595 nm, in which  $\text{SDE}_{\text{max}} > 75\%$ . We note that here, the measurements of the SDE and  $\text{SDE}^*$  were performed at relatively low average input-photon rates going into the cryogenic AF-SNAP system,  $1.79 \times 10^5$  and  $1.82 \times 10^5 \text{ s}^{-1}$ , respectively.

As the flux of the input photons increases, the SDE would decrease. To characterize the SDE of the AF-SNAP at various input-photon rates, we measured the  $\text{SDE}_{\text{max}}$  as a function of the average input-photon rate (Section S10 of Supporting Information). Note that we used the oscilloscope to measure the  $\text{SDE}_{\text{max}}$  in Figure 3a with a sampling rate of 2.5 GS/s and a

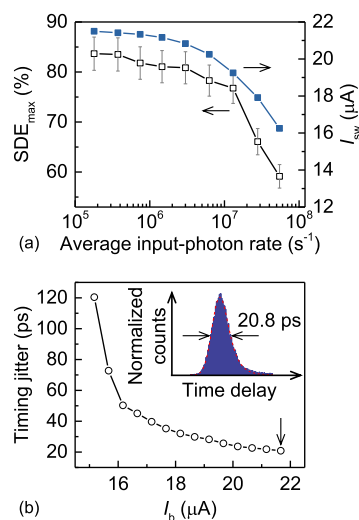


**Figure 3.** Timing properties of an arced fractal SNAP. (a) Measured  $\text{SDE}_{\text{max}}$  and the switching current,  $I_{\text{sw}}$ , as functions of the average input-photon rate. (b) Measured timing jitter as a function of the bias current,  $I_b$ . Inset: measured time-delay histogram at a bias current of 21.67  $\mu\text{A}$  and the EMG fitting, showing a full width at half maxima of a EMG fitting of 20.8 ps.

time span per frame of 1 ms because the maximum count rate of the input channel of the TAC is 12.5 Mcps, smaller than the photon-count rate we needed in this measurement. As the flux of the incident photon increases, the switching current decreases. Each value of  $\text{SDE}_{\text{max}}$  in Figure 3a is measured at a bias current of  $0.99I_{\text{sw}}$ . The results show that when the average input-photon rate increases to  $5.47 \times 10^7 \text{ s}^{-1}$ ,  $\text{SDE}_{\text{max}}$  drops to 59%, and the corresponding photon-count rate with the FCR excluded was 26 Mcps.

Figure 3b presents the measured timing jitter of the AF-SNAP by using a mode-locked fiber laser with a central wavelength of 1560 nm, a fast photodetector with 3 dB bandwidth of 40 GHz, and a real-time oscilloscope with a bandwidth of 4 GHz. The experimental setup is schematically presented in Section S11 of Supporting Information. Each data point in Figure 3b is the fwhm of the exponentially modified Gaussian (EMG) fitting<sup>47</sup> to the time-delay histograms [Figure S12b]. The lowest value of timing jitter was 20.8 ps at 21.67  $\mu\text{A}$ . The time-delay histogram and the EMG fitting is shown in the inset of Figure 3b. Timing jitter monotonically increased with decreasing the bias current in the avalanche regime, for example, at  $I_b = 19.67 \mu\text{A}$ , timing jitter increased to 25.6 ps. As for the other temporal properties, in the avalanche regime, the exponential fitting to the recovery edge of the output pulse shows a  $1/e$  time constant of 8.68 ns [Section S9 of Supporting Information].

We estimated the highest possible SDE for the current configuration of our system. The total transmittance of the two types of optical fibers connected through the mode-field adapter was measured to be 98% at ambient temperature; the coupling efficiency,  $\eta_c$ , between the high-index optical fiber and

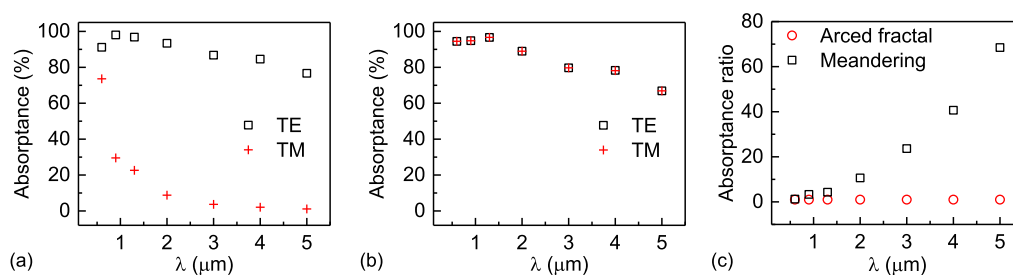


**Figure 4.** Simulated visible, near-infrared, and mid-infrared spectra of optical absorptance and the polarization dependence for the meandering and arced fractal SNSPDs. (a) Simulated optical absorptance of meandering SNSPDs for TE- and TM-polarization states. (b) Simulated optical absorptance of arced fractal SNSPDs for TE- and TM-polarization states. (c) Calculated absorptance ratios of TE- and TM-polarization states for meandering and arced fractal SNSPDs.

the photosensitive area was calculated to be 99%, assuming a perfect alignment; the optical absorptance,  $A$ , was simulated to be 96% at a wavelength of 1550 nm; and the internal quantum efficiency,  $P_r$ , was assumed to be 100%. The product of these numbers gives an estimation of the highest possible SDE to be 93%. The measured SDE, 84%, is less than this estimation of the highest possible SDE presumably because (1) certain misalignment between the optical mode and the photosensitive area existed in the package and (2)  $P_r$  was less than 100%.

The geometry of arced fractal nanowires can be applied to SNSPDs/SNAPs targeted for other interesting wavelengths by similarly re-designing the optical structures of the devices. In particular, the polarization dependence of SDE becomes more severe at longer wavelengths for meandering SNSPDs, and we think that the geometry presented in this work would be useful for creating SNSPDs working in the mid-infrared with low PS. We simulated and optimized the optical absorptance of meandering [Figure 4a] and arced fractal SNSPDs [Figure 4b] at some additional wavelengths, 0.6, 0.9, 1.3, 2, 3, 4, and 5 μm, for TE and TM polarization states. The optical structures are similar to that in Figure 1a except for that two, rather than three, pairs of alternating top layers maximize the optical absorptance of a meandering SNSPD for TE polarization and except for the modified thicknesses of the dielectric layers for different wavelengths. The simulation took into account the wavelength dependence of the refractive indices of the materials,<sup>48–50</sup> which are listed in Section S12 of Supporting Information. The calculated absorptance ratios of these two polarizations are presented in Figure 4c. At the longer wavelengths, the absorptance ratio for the meandering SNSPD increases, whereas the absorptance ratio for the arced fractal SNSPD remains constantly 1. As the polarization-dependent optical absorptance is the dominant contributor to the PS, and as this work demonstrates that the AF-SNAPs can reach a high SDE and high timing resolution at the near infrared, we think that arced fractal SNSPDs/SNAPs should be good device structures for polarization-insensitive single-photon detection in the mid-infrared, as well as the visible, spectral ranges.

## CONCLUSIONS

In conclusion, we demonstrated a fiber-coupled AF-SNAP with  $84 \pm 3\%$  SDE,  $1.02_{-0.02}^{+0.06}$  residual PS at a wavelength of 1575 nm, and 20.8 ps timing jitter. The SDE was boosted to the level comparable to the amorphous SNSPDs/SNAPs with low PS,<sup>4,32,35</sup> but the timing resolution of the NbTiN AF-SNAP exceeded (see Section S13 of Supporting Information for comparison; we also note that at their reported SDEs,

amorphous SNSPDs/SNAPs listed in Section S13 of Supporting Information exhibited lower DCR than the FCR and DCR of the NbTiN AF-SNAP that we report in this paper, but amorphous SNSPDs/SNAPs require lower temperatures). These combined properties have not been achieved with any single-photon detectors reported previously and are enabled by our comprehensive device design. In particular, the arced fractal geometry of the nanowires is the key enabling innovation that reduces the current-crowding effect and increases the switching current to the level comparable to that in the meandering SNSPDs and, therefore, enhances both SDE and timing resolution. Since the introduction of fractal SNSPDs in 2015,<sup>36</sup> although we kept enhancing their performances,<sup>29,37</sup> it had been elusive whether the fractal designs of the nanowires could be practical device structures; it is this work that gives a positive and unambiguous answer by showing that fractal SNSPDs are practical devices with excellent comprehensive performances, comparable to meandering SNSPDs, on top of which low PS is added. The arced fractal geometry is equally applicable to designing SNSPDs working in other spectral ranges, in particular, mid infrared. This demonstration is a detector coupled with a single-mode optical fiber, but the same geometry can be used for detectors coupled with few- or multi-mode optical fibers and for detecting single photons coming from the free space. Additionally, the negligibly small PS of the arced fractal SNSPDs/SNAPs would eliminate the security loophole, due to the polarization-dependent mismatch of the SDE, in the QKD systems.<sup>28</sup> We believe that this work paves the way for polarization-insensitive single-photon detection with high SDE and high timing resolution.

## ASSOCIATED CONTENT

### Supporting Information

The Supporting Information is available free of charge at <https://pubs.acs.org/doi/10.1021/acsp Photonics.1c00730>.

Distributions of supercurrent density in the meandering, standard fractal, and arced fractal SNSPDs; optical modes of the microcavity; nanofabrication process for making the detectors; measurements of the SDE and its polarization dependence; DCR and false-count rate; calibration of the optical attenuators; measurements of fiber end-facet reflectance; uncertainty analysis on the measured SDE and polarization sensitivity; output pulses in the avalanche and unstable regimes; measurements of the SDE at various input-photon rates; measurements of the timing jitter; refractive indices used in optical

simulation; and comparison of performances of SNSPDs with low polarization sensitivity (PDF)

## AUTHOR INFORMATION

### Corresponding Author

**Xiaolong Hu** – School of Precision Instrument and Optoelectronic Engineering, Tianjin University, Tianjin 300072, China; Key Laboratory of Optoelectronic Information Science and Technology, Ministry of Education, Tianjin 300072, China; [orcid.org/0000-0003-0269-8310](https://orcid.org/0000-0003-0269-8310); Email: [xiaolonghu@tju.edu.cn](mailto:xiaolonghu@tju.edu.cn)

### Authors

**Yun Meng** – School of Precision Instrument and Optoelectronic Engineering, Tianjin University, Tianjin 300072, China; Key Laboratory of Optoelectronic Information Science and Technology, Ministry of Education, Tianjin 300072, China

**Kai Zou** – School of Precision Instrument and Optoelectronic Engineering, Tianjin University, Tianjin 300072, China; Key Laboratory of Optoelectronic Information Science and Technology, Ministry of Education, Tianjin 300072, China

**Nan Hu** – School of Precision Instrument and Optoelectronic Engineering, Tianjin University, Tianjin 300072, China; Key Laboratory of Optoelectronic Information Science and Technology, Ministry of Education, Tianjin 300072, China

**Liang Xu** – School of Precision Instrument and Optoelectronic Engineering, Tianjin University, Tianjin 300072, China; Key Laboratory of Optoelectronic Information Science and Technology, Ministry of Education, Tianjin 300072, China

**Xiaojian Lan** – School of Precision Instrument and Optoelectronic Engineering, Tianjin University, Tianjin 300072, China; Key Laboratory of Optoelectronic Information Science and Technology, Ministry of Education, Tianjin 300072, China

**Stephan Steinhauer** – Department of Applied Physics, Royal Institute of Technology (KTH), Stockholm SE-106 91, Sweden; [orcid.org/0000-0001-6875-6849](https://orcid.org/0000-0001-6875-6849)

**Samuel Gyger** – Department of Applied Physics, Royal Institute of Technology (KTH), Stockholm SE-106 91, Sweden; [orcid.org/0000-0003-2080-9897](https://orcid.org/0000-0003-2080-9897)

**Val Zwiller** – Department of Applied Physics, Royal Institute of Technology (KTH), Stockholm SE-106 91, Sweden

Complete contact information is available at:

<https://pubs.acs.org/10.1021/acsp Photonics.1c00730>

### Author Contributions

Y.M., K.Z., and N.H. contributed equally to this work. X.H., Y.M., and K.Z. conceived the project. Y.M., K.Z., N.H., and X.H. designed the devices and performed numerical simulation. S.S., S.G., and V.Z. sputtered NbTiN films. K.Z., N.H., and X.L. fabricated the devices. Y.M. and L.X. performed the measurements. X.H., Y.M., K.Z., and N.H. analyzed the data and wrote the paper. All authors commented and revised the paper. X.H. supervised the project.

### Notes

The authors declare no competing financial interest.

## ACKNOWLEDGMENTS

The authors would like to thank Prof. Qing-Yuan Zhao at Nanjing University and Dr. Jin Chang at TU Delft for helpful discussions. This work was supported by the National Natural

Science Foundation of China (NSFC) (62071322, 11527808, and 61505141); National Key Research and Development Program of China (2019YFB2203600); and Natural Science Foundation of Tianjin City (19JCYBJC16900).

## REFERENCES

- (1) Marsili, F.; Verma, V. B.; Stern, J. A.; Harrington, S.; Lita, A. E.; Gerrits, T.; Vayshenker, I.; Baek, B.; Shaw, M. D.; Mirin, R. P.; Nam, S. W. Detecting single infrared photons with 93% system efficiency. *Nat. Photonics* **2013**, *7*, 210–214.
- (2) Esmaeil Zadeh, I.; Los, J. W. N.; Gourgues, R. B. M.; Steinmetz, V.; Bulgarini, G.; Dobrovolskiy, S. M.; Zwiller, V.; Dorenbos, S. N. Single-photon detectors combining high efficiency, high detection rates, and ultra-high timing resolution. *APL Photonics* **2017**, *2*, 111301.
- (3) Zhang, W.; You, L.; Li, H.; Huang, J.; Lv, C.; Zhang, L.; Liu, X.; Wu, J.; Wang, Z.; Xie, X. NbN superconducting nanowire single photon detector with efficiency over 90% at 1550 nm wavelength operational at compact cryocooler temperature. *Sci. China: Phys., Mech. Astron.* **2017**, *60*, 120314.
- (4) Reddy, D. V.; Nerem, R. R.; Lita, A. E.; Nam, S. W.; Mirin, R. P.; Verma, V. B. Exceeding 95% system efficiency within the telecom C-band in superconducting nanowire single photon detectors. *CLEO: QELS Fundamental Science*; Optical Society of America, 2019; paper FF1A–3.
- (5) Reddy, D. V.; Nerem, R. R.; Nam, S. W.; Mirin, R. P.; Verma, V. B. Superconducting nanowire single-photon detectors with 98% system detection efficiency at 1550 nm. *Optica* **2020**, *7*, 1649.
- (6) Chang, J.; Los, J. W. N.; Tenorio-Pearl, J. O.; Noordzij, N.; Gourgues, R.; Guardiani, A.; Zichi, J. R.; Pereira, S. F.; Urbach, H. P.; Zwiller, V.; Dorenbos, S. N.; Esmaeil Zadeh, I. Detecting telecom single photons with (99.5<sup>+0.5</sup><sub>-2.07</sub>)% system detection efficiency and high time resolution. *APL Photonics* **2021**, *6*, 036114.
- (7) Hu, P.; Li, H.; You, L.; Wang, H.; Xiao, Y.; Huang, J.; Yang, X.; Zhang, W.; Wang, Z.; Xie, X. Detecting single infrared photons toward optimal system detection efficiency. *Opt. Express* **2020**, *28*, 36884.
- (8) Hochberg, Y.; Charaev, I.; Nam, S.-W.; Verma, V.; Colangelo, M.; Berggren, K. K. Detecting sub-GeV dark matter with superconducting nanowires. *Phys. Rev. Lett.* **2019**, *123*, 151802.
- (9) Zhao, Q.; Jia, T.; Gu, M.; Wan, C.; Zhang, L.; Xu, W.; Kang, L.; Chen, J.; Wu, P. Counting rate enhancements in superconducting nanowire single-photon detectors with improved readout circuits. *Opt. Lett.* **2014**, *39*, 1869–1872.
- (10) Münzberg, J.; Vetter, A.; Beutel, F.; Hartmann, W.; Ferrari, S.; Pernice, W. H. P.; Rockstuhl, C. Superconducting nanowire single-photon detector implemented in a 2D photonic crystal cavity. *Optica* **2018**, *5*, 658–665.
- (11) Tao, X.; Chen, S.; Chen, Y.; Wang, L.; Li, X.; Tu, X.; Jia, X.; Zhao, Q.; Zhang, L.; Kang, L.; Wu, P. A high speed and high efficiency superconducting photon number resolving detector. *Supercond. Sci. Technol.* **2019**, *32*, 064002.
- (12) Zhang, W.; Huang, J.; Zhang, C.; You, L.; Lv, C.; Zhang, L.; Li, H.; Wang, Z.; Xie, X. A 16-pixel interleaved superconducting nanowire single-photon detector array with a maximum count rate exceeding 1.5 GHz. *IEEE Trans. Appl. Supercond.* **2019**, *29*, 2200204.
- (13) Korzh, B.; et al. Demonstration of sub-3 ps temporal resolution with a superconducting nanowire single-photon detector. *Nat. Photonics* **2020**, *14*, 250–255.
- (14) Esmaeil Zadeh, I.; et al. Efficient single-photon detection with 7.7 ps time resolution for photon correlation measurements. *ACS Photonics* **2020**, *7*, 1780–1787.
- (15) Marsili, F.; Bellei, F.; Najafi, F.; Dane, A. E.; Dauler, E. A.; Molnar, R. J.; Berggren, K. K. Efficient Single Photon Detection from 500 nm to 5  $\mu$ m Wavelength. *Nano Lett.* **2012**, *12*, 4799–4804.
- (16) Verma, V. B.; Lita, A. E.; Korzh, B. A.; Wollman, E.; Shaw, M.; Mirin, R. P.; Nam, S.-W. Towards single-photon spectroscopy in the mid-infrared using superconducting nanowire single-photon detec-

tors. *Advanced Photon Counting Techniques XIII*; International Society for Optics and Photonics, 2019. paper 109780N.

(17) Chen, Q.; Ge, R.; Zhang, L.; Li, F.; Zhang, B.; Jin, F.; Han, H.; Dai, Y.; He, G.; Fei, Y.; Wang, X.; Wang, H.; Jia, X.; Zhao, Q.; Tu, X.; Kang, L.; Chen, J.; Wu, P. Mid-infrared single photon detector with superconductor  $\text{Mo}_{0.8}\text{Si}_{0.2}$  nanowire. *Sci. Bull.* **2021**, *66*, 965–968.

(18) Zhang, X.; Wang, Q.; Schilling, A. Superconducting single X-ray photon detector based on  $\text{W}_{0.8}\text{Si}_{0.2}$ . *AIP Adv.* **2016**, *6*, 115104.

(19) Gol'tsman, G. N.; Okunev, O.; Chulkova, G.; Lipatov, A.; Semenov, A.; Smirnov, K.; Voronov, B.; Dzardanov, A.; Williams, C.; Sobolewski, R. Picosecond superconducting single-photon optical detector. *Appl. Phys. Lett.* **2001**, *79*, 705–707.

(20) Hadfield, R. H. single-photon detectors for optical quantum information applications. *Nat. Photonics* **2009**, *3*, 696–705.

(21) Taylor, G. G.; Morozov, D.; Gemmell, N. R.; Erotokritou, K.; Miki, S.; Terai, H.; Hadfield, R. H. Photon counting LIDAR at 2.3  $\mu\text{m}$  wavelength with superconducting nanowires. *Opt. Express* **2019**, *27*, 38147–38158.

(22) Gemmell, N. R.; McCarthy, A.; Liu, B.; Tanner, M. G.; Dorenbos, S. D.; Zwiller, V.; Patterson, M. S.; Buller, G. S.; Wilson, B. C.; Hadfield, R. H. Singlet oxygen luminescence detection with a fiber-coupled superconducting nanowire single-photon detector. *Opt. Express* **2013**, *21*, 5005–5013.

(23) Yin, H.-L.; et al. Measurement-device-independent quantum key distribution over a 404 km optical fiber. *Phys. Rev. Lett.* **2016**, *117*, 190501.

(24) Wang, H.; Qin, J.; Ding, X.; Chen, M.-C.; Chen, S.; You, X.; He, Y.-M.; Jiang, X.; You, L.; Wang, Z.; Schneider, C.; Renema, J. J.; Höfling, S.; Lu, C.-Y.; Pan, J.-W. Boson sampling with 20 input photons and a 60-mode interferometer in a  $10^{14}$ -dimensional Hilbert space. *Phys. Rev. Lett.* **2019**, *123*, 250503.

(25) Zhong, H.-S.; et al. Quantum computational advantage using photons. *Science* **2020**, *370*, 1460–1463.

(26) Zou, K.; Meng, Y.; Wang, Z.; Hu, X. Superconducting nanowire multi-photon detectors enabled by current reservoirs. *Photonics Res.* **2020**, *8*, 601–609.

(27) Zou, K.; Meng, Y.; Xu, L.; Hu, N.; Wang, Z.; Hu, X. Superconducting nanowire photon-number-resolving detectors integrated with current reservoirs. *Phys. Rev. Appl.* **2020**, *14*, 044029.

(28) Wei, K.; Zhang, W.; Tang, Y. L.; You, L.; Xu, F. Implementation security of quantum key distribution due to polarization-dependent efficiency mismatch. *Phys. Rev. A* **2019**, *100*, 022325.

(29) Meng, Y.; Zou, K.; Hu, N.; Lan, X.; Xu, L.; Zichi, J.; Steinhauer, S.; Zwiller, V.; Hu, X. Fractal superconducting nanowire avalanche photodetector at 1550 nm with 60% system detection efficiency and 1.05 polarization sensitivity. *Opt. Lett.* **2020**, *45*, 471.

(30) Dorenbos, S. N.; Reiger, E. M.; Akopian, N.; Perinetti, U.; Zwiller, V.; Zijlstra, T.; Klapwijk, T. M. Superconducting single photon detectors with minimized polarization dependence. *Appl. Phys. Lett.* **2008**, *93*, 161102.

(31) Huang, J.; Zhang, W. J.; You, L. X.; Liu, X. Y.; Guo, Q.; Wang, Y.; Zhang, L.; Yang, X. Y.; Li, H.; Wang, Z.; Xie, X. M. Spiral superconducting nanowire single-photon detector with efficiency over 50% at 1550 nm wavelength. *Supercond. Sci. Technol.* **2017**, *30*, 074004.

(32) Verma, V. B.; Marsili, F.; Harrington, S.; Lita, A. E.; Mirin, R. P.; Nam, S. W. A three-dimensional, polarization-insensitive superconducting nanowire avalanche photodetector. *Appl. Phys. Lett.* **2012**, *101*, 251114.

(33) Xu, R.; Zheng, F.; Qin, D.; Yan, X.; Zhu, G.; Kang, L.; Zhang, L.; Jia, X.; Tu, X.; Jin, B.; Xu, W.; Chen, J.; Wu, P. Demonstration of polarization-insensitive superconducting nanowire single-photon detector with Si compensation layer. *J. Lightwave Technol.* **2017**, *35*, 4707.

(34) Mukhtarova, A.; Redaelli, L.; Hazra, D.; Machhadani, H.; Lequien, S.; Hofheinz, M.; Thomassin, J.-L.; Gustavo, F.; Zichi, J.; Zwiller, V.; Monroy, E.; Gérard, J.-M. Polarization-insensitive fiber-

coupled superconducting-nanowire single photon detector using a high-index dielectric capping layer. *Opt. Express* **2018**, *26*, 17697.

(35) Verma, V. B.; Korzh, B.; Bussièrès, F.; Horansky, R. D.; Dyer, S. D.; Lita, A. E.; Vayshenker, I.; Marsili, F.; Shaw, M. D.; Zbinden, H.; Mirin, R. P.; Nam, S. W. High-efficiency superconducting nanowire single-photon detectors fabricated from MoSi thin-films. *Opt. Express* **2015**, *23*, 33792–33801.

(36) Gu, C.; Cheng, Y.; Zhu, X.; Hu, X. Fractal-Inspired, Polarization-Insensitive Superconducting Nanowire Single-Photon Detectors. *Novel Optical Materials and Applications*; Optical Society of America, 2015. paper JM3A.10.

(37) Chi, X.; Zou, K.; Gu, C.; Zichi, J.; Cheng, Y.; Hu, N.; Lan, X.; Chen, S.; Lin, Z.; Zwiller, V.; Hu, X. Fractal superconducting nanowire single-photon detectors with reduced polarization sensitivity. *Opt. Lett.* **2018**, *43*, 5017.

(38) We note that some researchers define PS as  $(\text{SDE}_{\text{max}} - \text{SDE}_{\text{min}})/(\text{SDE}_{\text{max}} + \text{SDE}_{\text{min}})$ , for example, in refs 30 and 34, which can be equivalently used for characterizing the polarization dependence of the detection efficiency.

(39) Clem, J. R.; Berggren, K. K. Geometry-dependent critical currents in superconducting nanocircuits. *Phys. Rev. B* **2011**, *84*, 174510.

(40) Su, H. T.; Wang, Y.; Huang, F.; Lancaster, M. J. Superconducting delay lines. *J. Supercond. Novel Magn.* **2008**, *21*, 7–16.

(41) Zichi, J.; Chang, J.; Steinhauer, S.; von Fieandt, K.; Los, J. W. N.; Visser, G.; Kalhor, N.; Lettner, T.; Elshaari, A. W.; Esmaeil Zadeh, I.; Zwiller, V. Optimizing the stoichiometry of ultrathin NbTiN films for high-performance superconducting nanowire single-photon detectors. *Opt. Express* **2019**, *27*, 26579.

(42) Miller, A. J.; Lita, A. E.; Calkins, B.; Vayshenker, I.; Gruber, S. M.; Nam, S. W. Compact cryogenic self-aligning fiber-to-detector coupling with losses below one percent. *Opt. Express* **2011**, *19*, 9102.

(43) Miki, S.; Yabuno, M.; Yamashita, T.; Terai, H. Stable, high-performance operation of a fiber-coupled superconducting nanowire avalanche photon detector. *Opt. Express* **2017**, *25*, 6796–6804.

(44) Chen, S.; You, L.; Zhang, W.; Yang, X.; Li, H.; Zhang, L.; Wang, Z.; Xie, X. Dark counts of superconducting nanowire single-photon detector under illumination. *Opt. Express* **2015**, *23*, 10786–10793.

(45) Gerrits, T.; Migdall, A.; Bienfang, J. C.; Lehman, J.; Nam, S. W.; Splett, J.; Vayshenker, I.; Wang, J. Calibration of free-space and fiber-coupled single-photon detectors. *Metrologia* **2019**, *57*, 015002.

(46) Marsili, F.; Najafi, F.; Dauber, E.; Molnar, R. J.; Berggren, K. K. Afterpulsing and instability in superconducting nanowire avalanche photodetectors. *Appl. Phys. Lett.* **2012**, *100*, 112601.

(47) Sidorova, M.; Semenov, A.; Hübers, H.-W.; Charaev, I.; Kuzmin, A.; Doerner, S.; Siegel, M. Physical mechanisms of timing jitter in photon detection by current-carrying superconducting nanowires. *Phys. Rev. B* **2017**, *96*, 184504.

(48) Palik, E. D. *Handbook of Optical Constants of Solids*; Academic Press: Boston, 1985.

(49) Hu, X. Efficient superconducting-nanowire single-photon detectors and their applications in quantum optics. Ph.D. Thesis, Massachusetts Institute of Technology, 2011.

(50) Bright, T. J.; Watjen, J. I.; Zhang, Z. M.; Muratore, C.; Voevodin, A. A.; Koukis, D. I.; Tanner, D. B.; Arenas, D. J. Infrared optical properties of amorphous and nanocrystalline  $\text{Ta}_2\text{O}_5$  thin films. *J. Appl. Phys.* **2013**, *114*, 083515.